

Elucidating the Factors Limiting the Photovoltaic Performance of Mixed Sb–Bi Halide Elpasolite Absorbers

Zewei Li, Yi-Teng Huang, Lokeshwari Mohan, Szymon J. Zelewski, Richard H. Friend, Joe Briscoe, and Robert L. Z. Hoye*

Although $\text{Cs}_2\text{AgBiBr}_6$ halide elpasolites have gained substantial attention as potential nontoxic and stable alternatives to lead–halide perovskites, they are limited by their wide bandgaps >2.2 eV. Alloying with Sb into the pnictogen site has been shown to be an effective method to lower the bandgap, but this has not translated into improvements in photovoltaic (PV) performance. Herein, the underlying causes are investigated. Pinhole-free films of $\text{Cs}_2\text{Ag}(\text{Sb}_x\text{Bi}_{1-x})\text{Br}_6$ are achieved through antisolvent dripping, but PV devices still exhibit a reduction in power conversion efficiency from $0.44\% \pm 0.02\%$ (without Sb) to $0.073\% \pm 0.007\%$ (90% Sb; lowest bandgap). There is a 0.7 V reduction in the open-circuit voltage, which correlates with the appearance of a sub-bandgap state ≈ 0.7 eV below the optical bandgap in the Sb-containing elpasolite films, as found in both absorbance and photoluminescence measurements. Through detailed Williamson–Hall analysis, it is found that adding Sb into the elpasolite films leads to an increase in film strain. This strain is relieved through aerosol-assisted solvent treatment, which reduces both the sub-bandgap state density and energetic disorder in the films, as well as reducing the fast early decay in the photogenerated carrier population due to trap filling. This work shows that Sb alloying leads to the introduction of extra sub-bandgap states that limit the PV performance, but can be mitigated through post-annealing treatment to reduce disorder and strain.

optoelectronics is $\text{Cs}_2\text{AgBiBr}_6$, which has been found to have long charge-carrier lifetimes exceeding 100 ns (in thin films),^[6–9] although recent studies have suggested that this is due to the detrimental formation of small polarons.^[10–13] Apart from questions around charge-carrier transport, an important limitation with $\text{Cs}_2\text{AgBiBr}_6$ is that its bandgap (2.25 eV)^[14] exceeds the optimal values for single-junction photovoltaics (PVs), indoor PVs, as well as top-cells for tandem PVs.^[15–19] Partly because of the wide, indirect bandgap, attempts at fabricating single-junction PVs have yielded power conversion efficiencies (PCEs) up to only 4.23%,^[20] with most reports $<3\%$.^[21–24] Indeed, there is still much variation in the PCEs reported for $\text{Cs}_2\text{AgBiBr}_6$ solar cells between different groups, suggesting that not all parameters influencing performance have yet been uncovered or are yet well controlled.

While reductions in the bandgap of $\text{Cs}_2\text{AgBiBr}_6$ could be achieved by exchanging the bromide for iodide, $\text{Cs}_2\text{AgBiI}_6$ is unstable against decomposition and there-

fore challenging to synthesize.^[25] A very recent study showed that a promising route to enhancing light absorption is through hydrogenation of $\text{Cs}_2\text{AgBiBr}_6$, and this led to solar cells with a stabilized power output efficiency of 6.25%.^[26] Another alternative that has been considered by several groups is to alloy Sb into the pnictogen site, which leads to bandgap bowing, such that the lowest bandgap (of 2.08 eV in thin films) is achieved with

1. Introduction


Halide elpasolites (also referred to as double perovskites) have gained substantial attention over the past few years because they are structurally analogous to the lead–halide perovskites, but are free from toxic regulated elements, and are structurally stable in ambient air.^[1–5] The most popular of these elpasolites for

Z. Li, Y.-T. Huang, S. J. Zelewski, R. H. Friend
Cavendish Laboratory
University of Cambridge
Cambridge CB3 0HE, UK

L. Mohan, J. Briscoe
School of Engineering and Materials Science and Materials Research
Institute
Queen Mary University of London
London E1 4NS, UK

S. J. Zelewski
Department of Semiconductor Materials Engineering
Faculty of Fundamental Problems of Technology
Wrocław University of Science and Technology
50-370 Wrocław, Poland

R. L. Z. Hoye
Department of Materials
Imperial College London
London SW7 2AZ, UK
E-mail: r.hoye@imperial.ac.uk

 The ORCID identification number(s) for the author(s) of this article can be found under <https://doi.org/10.1002/solr.202200749>.

© 2022 The Authors. Solar RRL published by Wiley-VCH GmbH. This is an open access article under the terms of the Creative Commons Attribution License, which permits use, distribution and reproduction in any medium, provided the original work is properly cited.

DOI: 10.1002/solr.202200749

$\text{Cs}_2\text{AgSb}_{0.9}\text{Bi}_{0.1}\text{Br}_6$, rather than $\text{Cs}_2\text{AgSbBr}_6$.^[14] Smaller bandgaps have been reported in bulk powders and single crystals, with values as low as 1.55 eV reported.^[27,28] Preliminary attempts have been made to investigate whether these reductions in bandgap could be translated into improvements in PV performance. However, groups have thus far reported that Sb alloying leads to a reduction in the PCE from >1% for $\text{Cs}_2\text{AgBiBr}_6$ down to <0.3% for alloyed Sb–Bi elpasolite absorbers.^[21–23] In particular, across multiple reports, it has been found that instead of improving the short-circuit current density (J_{SC}), introducing Sb into $\text{Cs}_2\text{AgBiBr}_6$ results in reductions in J_{SC} , and with open-circuit voltages (V_{OC} s) well below E_{g}/q (losses exceeding 1.4 V), where E_{g} is the optical bandgap and q the elementary charge.^[21–23]

Herein, we investigate the factors behind the reduction in PV performance when alloying Sb into $\text{Cs}_2\text{AgBiBr}_6$. To determine whether these reductions in performance are due to shunting effects, we developed an antisolvent dripping method to tune the morphology of the $\text{Cs}_2\text{AgSb}_x\text{Bi}_{1-x}\text{Br}_6$ films. The bulk properties of these films were analyzed using detailed photoluminescence (PL) and absorbance (via photothermal deflection spectroscopy, or PDS) measurements, from which it was found that sub-bandgap states were introduced through Sb alloying that could account for the reductions in V_{OC} . We performed aerosol-assisted post-annealing treatments on the solution-processed films, and analyzed the effects on the density of sub-gap states and charge-carrier lifetime.

2. Results and Discussion

2.1. Photovoltaic Performance

Thin films were initially deposited by solution processing, following our previously reported approach.^[14] However, the film morphology was found to be noncontinuous, with many large

pinholes, especially in the films containing Sb (Figure 1a,b, and S1, Supporting Information). The mesoporous TiO_2 scaffold that the films were deposited onto was visible between the grains of the Sb-containing elpasolites, which formed an island-like morphology (Figure 1a,b). $\text{Cs}_2\text{AgBiBr}_6$ had a much smaller density of pinholes, and the morphology was comprised of interconnected grains (rather than an island-like microstructure), albeit with small pinholes forming at some grain boundaries (Figure 1c). When complete PV devices were fabricated (device structure: FTO/ TiO_2 /mesoporous TiO_2 / $\text{Cs}_2\text{AgSb}_x\text{Bi}_{1-x}\text{Br}_6$ /PTAA/Au, see Section 4), rectification was still obtained from $\text{Cs}_2\text{AgBiBr}_6$, with a fill factor (FF) of $58\% \pm 3\%$ (Table 1). However, for $\text{Cs}_2\text{AgSbBr}_6$ and $\text{Cs}_2\text{AgSb}_{0.9}\text{Bi}_{0.1}\text{Br}_6$, the FFs were 50% or below, and the PCEs of the devices were below 0.1% (Table 1).

To ensure that shunting due to pinholes in the Sb-containing elpasolite films did not limit PV performance, we investigated the use of antisolvent dripping to improve film morphology. This approach has been widely used in spin-coated lead–halide perovskites to achieve films without pinholes.^[29,30] In this method, an antisolvent with low solubility for the double perovskite or inorganic-solvent complex intermediates is dropped onto

Table 1. Photovoltaic device performance of $\text{Cs}_2\text{AgSb}_x\text{Bi}_{1-x}\text{Br}_6$ thin films. For films deposited with the use of toluene antisolvent, this was dropped 15 s after the start of spinning.

Sb fraction	Antisolvent?	V_{OC} [V]	J_{SC} [mA cm^{-2}]	FF [%]	PCE [%]
0	No	1.17 ± 0.02	-0.64 ± 0.02	58 ± 3	0.44 ± 0.02
0.9	Yes	0.46 ± 0.01	-0.32 ± 0.01	49 ± 2	0.073 ± 0.007
0.9	No	0.45 ± 0.02	-0.41 ± 0.02	51 ± 1	0.09 ± 0.01
1.0	Yes	0.42 ± 0.01	-0.08 ± 0.02	41 ± 4	0.014 ± 0.004
1.0	No	0.3 ± 0.1	-0.09 ± 0.01	40 ± 10	0.015 ± 0.009

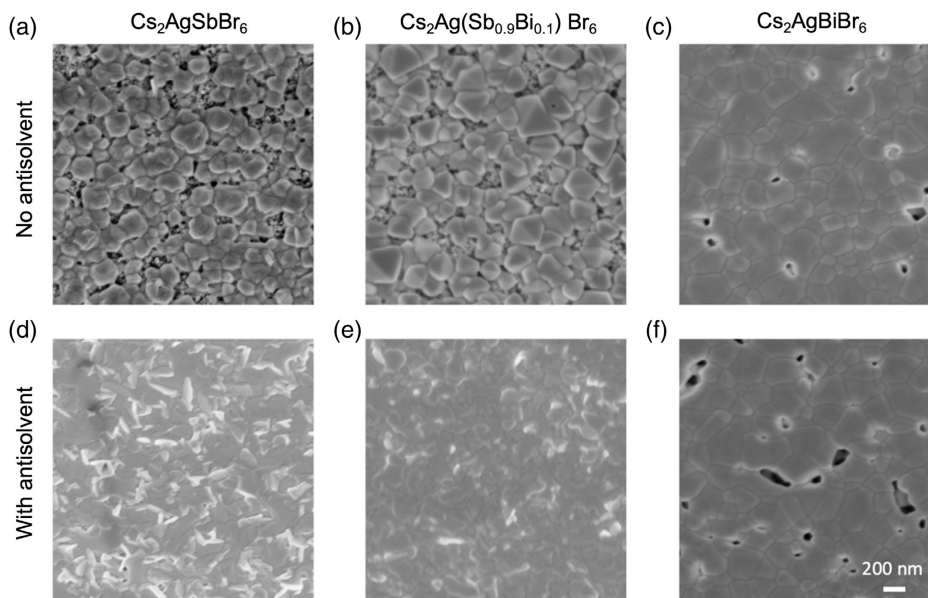


Figure 1. Scanning electron micrographs of: a,d) $\text{Cs}_2\text{AgSbBr}_6$, b,e) $\text{Cs}_2\text{Ag}(\text{Sb}_{0.9}\text{Bi}_{0.1})\text{Br}_6$, and c,f) $\text{Cs}_2\text{AgBiBr}_6$ thin films deposited onto glass/FTO/compact TiO_2 /mesoporous TiO_2 substrates. The films were prepared (a–c) without and (d–f) with toluene antisolvent dripping during growth.

the spinning film. This washes away the original solvent (dimethyl sulfoxide, or DMSO), inducing rapid supersaturation. As a result, a high density of nuclei is formed, which improves the likelihood of the microstructure being free from pinholes.^[31] We compared the commonly used low-polarity antisolvents used with polar inorganic compounds (toluene, chlorobenzene, and chloroform), as well as ethanol (in which we found $\text{Cs}_2\text{AgBiBr}_6$ to have low solubility). From these, we found that toluene was the most effective (see Section 4 for details on the processing). In the cases of $\text{Cs}_2\text{AgSbBr}_6$ and $\text{Cs}_2\text{AgSb}_{0.9}\text{Bi}_{0.1}\text{Br}_6$ shown in Figure 1, it can be seen that the morphology changed from island-like (no antisolvent) to continuous (with toluene antisolvent), thus eliminating pinholes from the areas analyzed. However, the use of toluene antisolvent for $\text{Cs}_2\text{AgBiBr}_6$ led to no improvements in film morphology (Figure 1c,f). Therefore, for $\text{Cs}_2\text{AgBiBr}_6$ PVs, we used absorber layers deposited without antisolvent treatment.

Despite the improvements in film morphology, the PV devices based on Sb-containing films did not improve in PCE following antisolvent treatment (Table 1). Indeed, the PCE remained an order of magnitude lower than that of $\text{Cs}_2\text{AgBiBr}_6$ PVs, despite the antisolvent-treated Sb-containing films having fewer pinholes. This suggests that the differences in PV performance may be related to properties of the bulk of the materials, rather than differences in morphology.

Examining the PV performance shown in Figure 2 in detail, it is noteworthy that the PV devices based on $\text{Cs}_2\text{AgSbBr}_6$ and $\text{Cs}_2\text{AgSb}_{0.9}\text{Bi}_{0.1}\text{Br}_6$ had V_{OC} s ≈ 0.7 V below the V_{OC} of $\text{Cs}_2\text{AgBiBr}_6$ PVs (Figure 2a, Table 1). This substantial reduction

in V_{OC} is consistent with increases in the reverse-bias dark current density by over an order of magnitude at -0.2 V applied bias with the addition of Sb (Figure 2b). These results suggest that loss channels are introduced to the devices with Sb-containing films. Note that the dark currents could not be measured at reverse biases beyond -0.2 V owing to diode breakdown.

Furthermore, in increasing the Sb content of the elpasolite films from 0% to 90% and 100%, there was a monotonic decrease in the J_{SC} (Figure 2a, Table 1), which is consistent with increased nonradiative recombination. The trends in J_{SC} were also consistent with those of the external quantum efficiency (EQE) measurements, in which EQE values decreased with increasing Sb content (Figure 2c). The integrated J_{SC} s from EQE measurements were 0.87 (100% Bi), 0.22 (90% Sb), and 0.03 mA cm^{-2} (100% Sb), which are close to the measured J_{SC} values shown in Table 1.

It is notable that the EQE curve for the $\text{Cs}_2\text{AgBiBr}_6$ PV device exhibited a clear peak centered at 2.8 eV (Figure 2c), which is consistent with the sharp peak in the optical absorption spectrum (see Ref. [14]) that has been attributed to the concentrated states in the conduction band, as well as excitonic features.^[14,32] With increasing Sb content, this peak in the EQE spectrum becomes less pronounced (Figure 2c), in agreement with our previous measurements of the absorption spectra of the films, in which these sharp features become obscured due to the broadening arising from increased disorder in the films.^[14] In plotting the EQE spectra on a log-linear scale (Figure 2d), we can more clearly observe the onset of EQE. From these plots, we can see that the PVs based on films containing 90% Sb had the lowest onset, which

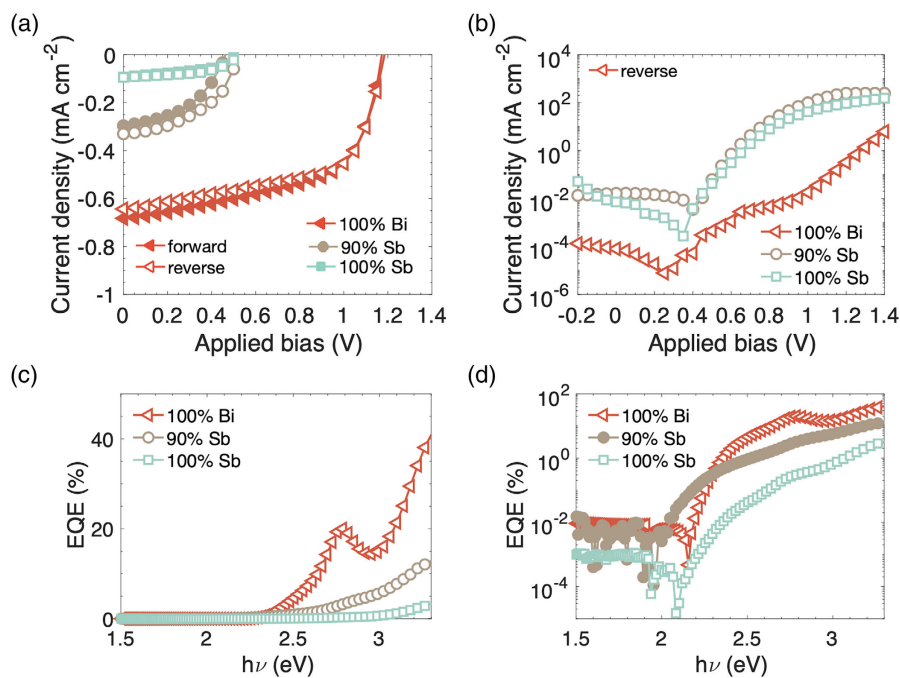


Figure 2. Photovoltaic performance of $\text{Cs}_2\text{AgSb}_x\text{Bi}_{1-x}\text{Br}_6$ thin films. a) Current density (J) versus voltage (V) curves measured under 1 sun illumination (filled: forward sweep, open: reverse sweep), b) J - V curves measured in the dark (reverse sweep only). A comparison of the forward and reverse sweeps of the dark J - V curves are shown in Figure S2, Supporting Information. c) External quantum efficiency (EQE) of the photovoltaic devices and d) log-linear plot of the EQE spectrum. Note: the 100% Bi sample was not antisolvent treated, whilst the Sb-containing samples were to compare films with the best morphology.

is in agreement with these materials having the smallest optical bandgap.^[14] However, despite the reductions in the optical bandgap, there was no improvement in performance due to the loss channels introduced with Sb alloying, as well as the low absorption coefficients near the indirect bandgaps of these materials. These results all together suggest that the performance of Sb-containing elpasolites is limited by the bulk properties, rather than the morphology. Therefore, in subsequent sections, we analyze the optical and structural properties of the bulk in detail, focusing consistently on films prepared without antisolvent treatment.

2.2. Optical Loss Characterization

To understand the cause of the loss channels introduced to the PV devices through the addition of Sb into the elpasolite films, we measured the sub-bandgap absorbance through photothermal deflection spectroscopy (PDS; Figure 3a), as well as the photoluminescence (PL) spectra of the bare films (Figure 3b). From

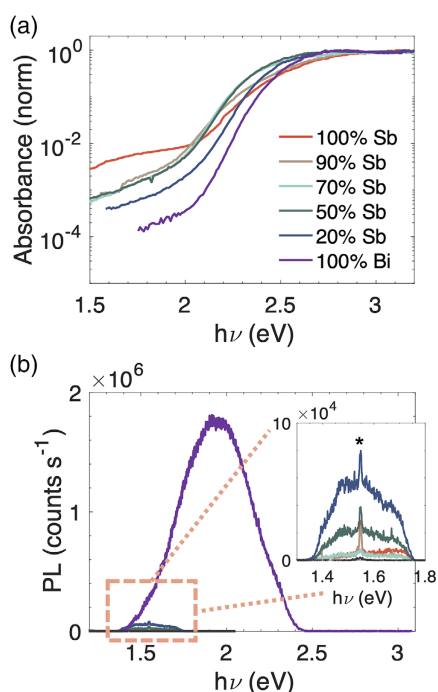


Figure 3. Effect of Sb composition on the: a) sub-bandgap absorbance measured by photothermal deflection spectroscopy and b) photoluminescence (PL) spectra, with excitation from a pulsed 400 nm wavelength source. The legend for part (b) is the same as for part (a). The data in part (a) were collected in our previous work in Ref. [14], and are replotted here. The data in part (b) are original. The PL spectrum of the glass substrate the films was deposited onto is also given in black. The peak in the inset marked with an asterisk is from the original laser (800 nm wavelength). The PL measurements were taken using an intensified charge-coupled device (iCCD) camera, with the grating centered at 900 nm wavelength (1.38 eV) to measure the full PL spectrum of the Sb-containing films (Figure 3b, inset). However, this resulted in a cut-off at 1.77 eV, preventing the full PL spectrum of Cs₂AgBiBr₆ to be measured. Cs₂AgBiBr₆ was therefore re-measured with the grating centered at 700 nm wavelength, and this PL spectrum scaled to be compared with the other measurements shown here (details in Figure S4, Supporting Information). Note: samples in this figure were not antisolvent treated.

the PDS spectra, it can be seen that as the Sb content of the bare elpasolite films increased, there was a concomitant increase in the sub-bandgap absorbance, which originates at ≈ 1.55 eV. These measurements are consistent with the PL spectra, which showed that alloying Sb into Cs₂AgBiBr₆ led to the PL peak (originally centered at 1.94 eV) being substantially quenched and red-shifted to a broad peak centered at approximately between 1.5 and 1.55 eV (Figure 3b). These results all suggest that Sb-alloying leads to a sub-bandgap state being introduced that acts as a loss channel. Photogenerated charge carriers relax to this state, from which they weakly luminesce. These results agree with previous observations that Sb addition into Cs₂AgBiBr₆ quenches the PL.^[21] In addition, the sub-bandgap state located at 1.55 eV is 0.7 eV below the optical bandgap of Cs₂AgBiBr₆ (2.25 eV), which matches the 0.7 V loss in V_{OC} in the PV devices. That is, adding Sb into Cs₂AgBiBr₆ would lower the V_{OC} not only due to a reduction in bandgap (from 2.25 to 2.08 eV with 90% Sb)^[14] or increases in Urbach energy, but would also be substantially reduced by charge-carriers relaxing to the sub-bandgap state introduced (illustrated in Figure S3, Supporting Information).

2.3. Aerosol-Assisted Post-Annealing Treatment

We next investigated whether the density of sub-bandgap states in the Sb-containing elpasolites could be reduced through an aerosol-assisted post-annealing treatment. The aerosol treatment involves annealing thin films in a solvent-vapor-rich environment, created by flowing an aerosol of the solvent over the films at an optimized temperature and flow rate.^[33] The solvent vapors are insufficient for dissolving the thin film, but enable mass transport between grains, in which lower energy large grains grow at the expense of higher energy small grains.^[31,33] This Ostwald ripening process leads to the formation of larger grains, with improved crystallinity and uniformity in grain size, as well as reduced tensile strain in thin films.^[34] Aerosol annealing with lead-halide perovskites has been demonstrated to give rise to reduced nonradiative recombination, improved optoelectronic uniformity between grains, as well as improved performance in PVs and photodetectors.^[33,35]

To investigate the effect of aerosol annealing on the bulk optical and structural properties of the halide elpasolites, we again prepared films without antisolvent treatment. We used a 50:50 mixture of *N,N*-dimethylformamide (DMF) and DMSO for the aerosol, and annealed the films at temperatures from 100 to 150 °C for 5 min during the treatment. Following aerosol annealing, the films were annealed again at 150 °C in an inert N₂ environment (see Section 4). We focused on the 90% Sb alloy films because these are the lowest bandgap materials, and found that the optical bandgap (2.03 eV) and phase purity remained unchanged following aerosol annealing (Figure S5 and S6, Supporting Information, respectively). From PDS measurements, we found that the sub-bandgap absorbance decreased following aerosol annealing (Figure 4a), with the integrated area of the sub-bandgap absorbance monotonically reducing as the annealing temperature increased (Figure 4b). In particular, there was a steady decrease in the absorption onset at 1.55 eV as the aerosol annealing temperature increased (Figure 4a), suggesting

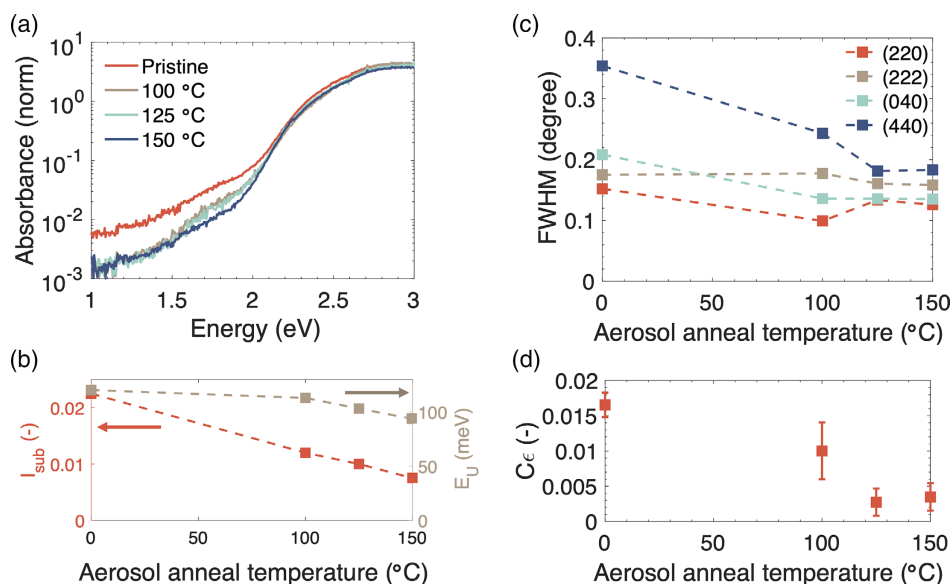


Figure 4. Effect of aerosol-assisted post-annealing on the sub-bandgap state density and crystallinity of the $\text{Cs}_2\text{AgSb}_{0.9}\text{Bi}_{0.1}\text{Br}_6$ films. a) Photothermal deflection spectroscopy (PDS) measurements of the absorbance and b) integrated sub-bandgap state intensity (I_{sub}) and Urbach energy (E_U) of the absorption edge. The bandgap was found to be 2.03 eV (Figure S5, Supporting Information), which is close to our previous report.^[14] c) Full-width at half maximum (FWHM) of the main diffraction peaks, and how they vary with the aerosol annealing temperature (see Figure S6, Supporting Information for diffraction patterns). d) Trend in the strain (ϵ) as a function of the aerosol annealing temperature, obtained from Williamson–Hall plots (Figure S7, Supporting Information). C is a constant. Errors bars represent one standard error. Note: the samples investigated were not antisolvent-treated during the deposition of the original films.

a decrease in the density of this sub-bandgap state. In addition, the Urbach energy reduced from 120 (pristine) to 94 meV (aerosol) annealed at 150 °C (Figure 4b), showing that aerosol annealing also reduced energetic disorder in these materials.

We analyzed the X-ray diffraction (XRD) patterns to understand the structural changes occurring following aerosol annealing. By profile fitting the XRD patterns (Figure S6, Supporting Information), we obtained the full width at half maxima (FWHM) of the diffraction peaks. From Figure 4c, it can be seen that there was an overall reduction in FWHM with an increase in the aerosol annealing temperature. This may be due to an increase in grain size (as previously found from aerosol-annealed lead–halide perovskite films),^[33,35] or a decrease in strain in the films. To decouple the effects of grain size and strain, we constructed Williamson–Hall plots for films annealed at each temperature (Figure S7, Supporting Information). It was found that the effects of strain dominated the effects of crystallite size, such that there was a clear reduction in the strain as annealing temperature increased (Figure 4d).

We note that we checked this analysis using the Scherrer equation to calculate the crystallite size from each diffraction peak for each sample, and averaging (Figure S8, Supporting Information). From this Scherrer analysis, we found no change in crystallite size between the different annealing temperatures. The error bars were also large, showing there to be significant variation in the crystallite sizes calculated from each diffraction peak for each sample. In addition, the crystallite sizes obtained were between 30 and 80 nm, which are well below the size of the features in the microstructure of the films (Figure 1). While it is possible that each feature in this microstructure is composed of multiple crystallites, as has been found with halide

perovskites,^[36] the large uncertainty and absence of a trend in crystallite size with aerosol annealing are consistent with the explanation that the broadening of the XRD patterns is dominated by the effects of changing strain. Indeed, it is possible that the grains are sufficiently large such that size broadening is significantly smaller than strain broadening, such that the crystallite size could not be easily extracted from a Williamson–Hall plot or Scherrer analysis of the films.

The aforementioned analysis, therefore, indicates that an important limiting factor of high Sb contents is the presence of strain in the films. We, therefore, reanalyzed the XRD patterns we previously took over the $\text{Cs}_2\text{AgSb}_x\text{Bi}_{1-x}\text{Br}_6$ composition series in ref. [14], focusing particularly on 0%, 90%, and 100% Sb (Figure S9, Supporting Information). From the Williamson–Hall plots (Figure S10a–c, Supporting Information), we found that strain did indeed increase with increasing Sb content (Figure S10d, Supporting Information). This may be due to Sb^{3+} having a smaller ionic radius (90 pm) than Bi^{3+} (117 pm) when octahedrally coordinated,^[37] such that introducing Sb to the pnictogen site may have caused local contractions of the lattice, and hence local strain fields with the introduction of defect states. Grains with clusters of Sb-containing pnictogen–halide octahedra could have a larger strain, owing to the combination of individual strain fields. These grains likely have higher energy, and aerosol annealing would then result in lower strain grains growing at the expense of higher strain, higher energy grains, thus leading to the reduction in film strain and defect density found.

Finally, we determined how aerosol annealing influenced the charge-carrier kinetics of the $\text{Cs}_2\text{AgSb}_{0.9}\text{Bi}_{0.1}\text{Br}_6$ films. For this,

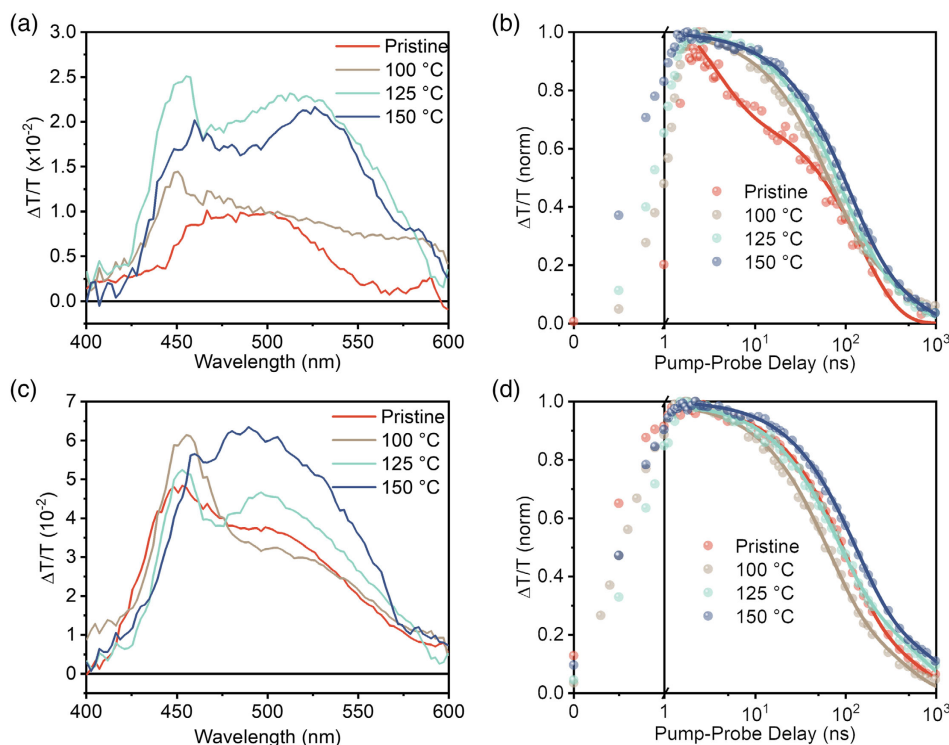


Figure 5. Effect of aerosol-annealing on the charge-carrier kinetics of $\text{Cs}_2\text{AgSb}_{0.9}\text{Bi}_{0.1}\text{Br}_6$ films. a,c) Transient absorption spectra at a pump-probe delay of 5 ns and b,d) ground state bleach kinetics over the wavelength range 420–560 nm, measured at a,b) 53 and c,d) 93 $\mu\text{J cm}^{-2} \text{ pulse}^{-1}$ fluence. The pump beam was a 355 nm wavelength laser with a repetition rate of 1 kHz, and the samples were measured in transmission, with pump and probe incident on the film surface. In parts (b) and (d), the data points are individually shown, whereas the fits are shown as solid lines (see Table 2). Note that both laser fluences used exceed that which would produce the same excess carrier density as 1 sun illumination (see Note S1, Supporting Information).

we used transient absorption (TA) spectroscopy, which measures the change in absorbance of the films following photoexcitation with a pulsed pump laser (355 nm wavelength). A positive relative change in transmittance ($\Delta T/T$) is due to photoexcited charge carriers occupying an empty state that existed before excitation (e.g., electrons in the conduction band), and this is the ground state bleach (GSB). From Figure 5a,c, it can be seen that the onset in GSB was at just below 600 nm wavelength (2.06 eV), in agreement with the measured optical bandgap of these materials (2.03 eV, Figure S5, Supporting Information). Photoinduced absorption (PIA) features are absent from these TA spectra, in contrast to $\text{Cs}_2\text{AgBiBr}_6$,^[38] and this allowed us to more clearly monitor the decay in the photo-excited carrier population. We integrated over 420–560 nm wavelength and measured the GSB kinetics (Figure 5b,d). At a low excitation fluence of 53 $\mu\text{J cm}^{-2} \text{ pulse}^{-1}$ (Figure 5a,b), the pristine sample decayed faster than the aerosol-annealed samples over the first 100 ns (Figure 5b). By contrast, under a high fluence of 93 $\mu\text{J cm}^{-2} \text{ pulse}^{-1}$, the pristine sample decayed in a comparable manner to the other samples (Figure 5d). Note that both of these fluences are above the laser fluence that would produce the same excess carrier density as 1 sun illumination (Note S1, Supporting Information), and we would therefore expect the faster early-stage decay in the photoexcited charge-carriers found in the lower fluence measurements to occur in the PV devices, which could limit performance.

These TA results are consistent with the pristine sample having a high sub-bandgap trap density. It is possible that under low fluence, the photoexcited carrier population rapidly relaxed to this sub-bandgap state, resulting in a depopulation of carriers in the conduction or valence bands. Indeed, in comparing the GSB spectra at a pump-probe delay of 5 ns (Figure 5a), it can be seen that the pristine sample had the lowest $\Delta T/T$ intensity, which is consistent with carrier depopulation. The sample aerosol annealed at 100 °C had the next lowest $\Delta T/T$ intensity, whereas the samples annealed at 125 and 150 °C had the highest intensities and were similar (Figure 5a). This is consistent with a steady reduction in sub-bandgap state density with increasing aerosol annealing temperature.

With an increase in excitation fluence, the pristine sample exhibited a marked increase in $\Delta T/T$ intensity (Figure 5c), especially at the low-energy edge. This is consistent with the sub-bandgap state being filled under high fluence, such that there was a slower depopulation of the excited state. We fit the GSB kinetics with a phenomenological biexponential model to numerically describe these decays to enable a quantitative comparison, and the fitted parameters are shown in Table 2. From these fits, we found a marked increase in the effective lifetime of the pristine sample when increasing the fluence (Table 2; see also Figure S11, Supporting Information), which is consistent with the earlier explanation made. But we also found that the samples aerosol annealed at the higher two temperatures

Table 2. Fitting parameters from a phenomenological biexponential fit to the GSB kinetics from TA measurements of pristine and aerosol-annealed $\text{Cs}_2\text{AgSb}_{0.9}\text{Bi}_{0.1}\text{Br}_6$ thin films. The model was $\frac{I}{I_0} = A_1 \exp\left(-\frac{t-t_0}{\tau_1}\right) + A_2 \exp\left(-\frac{t-t_0}{\tau_2}\right)$, where I/I_0 is the normalized GSB signal, A_1 and A_2 the pre-exponential constants, τ_1 and τ_2 the time constants of this model, and t_0 the time at which the GSB reaches its peak signal after photo-excitation. The effective time-constant τ_{eff} was the average between τ_1 and τ_2 , weighted by the pre-exponential constant.

Aerosol annealing temperature [°C]	Excitation fluence [$\mu\text{J cm}^{-2} \text{ pulse}^{-1}$]	A_1 [-]	τ_1 [ns]	A_2 [-]	τ_2 [ns]	τ_{eff} [ns]
None (pristine)	53	0.45	3.4	0.73	147	92
	93	0.62	58.0	0.31	388	239
100	53	0.61	60.4	0.29	477	196
	93	0.60	58.0	0.31	388	170
125	53	0.62	76.0	0.31	373	175
	93	0.56	74.2	0.34	652	292
150	53	0.65	99.1	0.26	469	205
	93	0.61	121.0	0.28	1027	406

of 125 and 150 °C also increased in lifetime with increasing fluence (Table 2 and Figure S11, Supporting Information), albeit with smaller differences than in the pristine sample. This was consistent with these samples also exhibiting higher $\Delta T/T$ intensities as the fluence increased, particularly at the low-energy edge (Figure 5a vs c). These results suggest that the sub-bandgap states in the materials aerosol annealed at higher temperatures were not eliminated, and that these materials still underwent a degree of carrier depopulation to the sub-bandgap states under low fluences.

3. Conclusion

In conclusion, we have found that alloying Sb into $\text{Cs}_2\text{AgBiBr}_6$ leads to a reduction in photovoltaic performance due to the introduction of sub-bandgap states ≈ 0.7 eV below the optical bandgap. Thus, although Sb alloying leads to a reduction in the bandgap of $\text{Cs}_2\text{AgBiBr}_6$, the V_{OC} is reduced by 0.7 V due to charge carriers depopulating the band states to the sub-bandgap state, leading to a reduction in the quasi-Fermi level splitting. The shorter charge-carrier lifetimes also lead to reduced EQEs, and hence lower J_{SC} s. Furthermore, the absorption strength at the indirect bandgap is low in these elpasolites, and the reductions in bandgap do not give a sizeable increase in EQE at longer wavelengths. Through detailed Williamson–Hall analysis, we found that introducing Sb into $\text{Cs}_2\text{AgBiBr}_6$ leads to an increase in strain in these films, which is likely due to the smaller size of the Sb^{3+} cation compared to the Bi^{3+} , and is a likely cause of the sub-bandgap state introduced. We found that we could relieve the strain introduced through aerosol annealing, and that this could reduce (but not eliminate) the density of sub-bandgap states, and slow down the depopulation of charge carriers from the excited state. This work shows the limitations of Sb alloying as a strategy to reduce the bandgap of $\text{Cs}_2\text{AgBiBr}_6$, and emphasizes the importance of controlling

strain in compositional engineering efforts to tune the properties of halide elpasolite films.

4. Experimental Section

Synthesis of $\text{Cs}_2\text{AgSb}_x\text{Bi}_{1-x}\text{Br}_6$ Thin Films: The procedure for synthesizing these films is based on our previously reported method reported in ref. [14]. Separate solutions containing Bi only, and Sb only were prepared in DMSO. For the precursor solution containing only Bi in the pnictogen site, 1.5 mmol CsBr (99.9%, Sigma Aldrich), 0.75 mmol AgBr (99.998%, Alfa Aesar), 0.75 mmol BiBr_3 (99.998%, Sigma Aldrich) were dissolved in 1.5 mL anhydrous DMSO (99.9%, Sigma Aldrich) and mixed at 700 rpm at room temperature inside an N_2 -filled glovebox for 1 h. For the precursor solution with only Sb in the pnictogen site, 0.75 mmol SbBr_3 (99.99%, Sigma Aldrich) was mixed with 1.5 mmol CsBr and 0.75 mmol AgBr. This solution was also mixed at 700 rpm at room temperature inside an N_2 -filled glovebox for an hour. Both solutions were subsequently filtered through a 0.2 μm PTFE membrane filter (Sigma Aldrich), and either directly used for growing $\text{Cs}_2\text{AgBiBr}_6$ and $\text{Cs}_2\text{AgSbBr}_6$, or mixed (450 μL Sb-based solution + 50 μL Bi-based solution) to achieve $\text{Cs}_2\text{AgSb}_{0.9}\text{Bi}_{0.1}\text{Br}_6$. It was previously shown that the nominal stoichiometry in solution matched the bulk composition of the films.^[14]

The substrates used for characterization were borosilicate glass (for PL measurements) or quartz (for XRD and PDS measurements). These substrates were cleaned by ultrasonication in acetone, followed by propan-2-ol, for 15 min each. Afterward, the substrates were dried by flowing compressed dry air before O_2 plasma treatment for 10 min (300 W forward power, 0 W reverse power). These substrates were subsequently taken inside an N_2 -filled glovebox and heated at 75 °C. The Sb-containing solutions were kept at room temperature, whereas the Bi-only solution was preheated to 75 °C on a hotplate. To deposit the films, the substrate was plated onto a vacuum-free check, and 60 μL solution was dropped immediately, before spinning at 4000 rpm for 45 s. $\text{Cs}_2\text{AgSbBr}_6$ and $\text{Cs}_2\text{AgSb}_{0.9}\text{Bi}_{0.1}\text{Br}_6$ were subsequently annealed at 135 °C for 5 min inside an N_2 -filled glovebox, whereas $\text{Cs}_2\text{AgBiBr}_6$ was annealed at 250 °C for 5 min. For the antisolvent-treated films, 150 μL of toluene was dropped quickly onto the spinning substrate 15 s after the start of spinning.

Photovoltaic Device Fabrication and Characterization: Fluorine-doped tin oxide (FTO) coated glass (Sigma Aldrich) was patterned by etching with 2 mol L^{-1} HCl (Fisher Chemical) and Zn powder (98%, Sigma Aldrich). The substrates were subsequently cut to 14 mm \times 14 mm squares and cleaned with 2% Hellmanex solution, being rinsed with deionized water and ethanol. They were cleaned in the same way as the glass/quartz substrates described earlier, but with 5 min of O_2 plasma treatment.

A blocking layer of TiO_2 was subsequently deposited by spray pyrolysis. The substrates were placed on a hotplate and heated up to 450 °C. For spray pyrolysis, the precursor solution was made by mixing 0.4 mL acetylacetone (99%, Alfa Aesar), 0.6 mL titanium diisopropoxide bis(acetylacetonate) (75 wt% in isopropanol, Sigma Aldrich) and 9 mL ethanol. The substrates were distributed over the hotplate, and the solution was evenly sprayed over the entire hotplate, with the tube held 20 cm away from the hotplate, at an angle of 45°. The spraying was repeated every 20 s, over a period of 20 min. The substrates were subsequently cooled naturally to 150 °C, before they were removed from the hotplate. To deposit the mesoporous TiO_2 layer, TiO_2 paste (Dyso) was dissolved in ethanol at 150 mg mL^{-1} . 30 μL of this solution was subsequently dropped onto the TiO_2 -coated FTO, then spun at 4000 rpm for 10 s. The substrates were annealed on a hotplate with a gradual ramp up in temperature (5 min ramp up to 125 °C, hold for 5 min, 15 min ramp up to 325 °C, hold for 5 min, 5 min ramp up to 375 °C, hold for 5 min, 5 min ramp up to 450 °C, hold for 30 min), before being naturally cooled to 150 °C and removed from the hotplate. The TiO_2 -coated substrates were immediately taken into an N_2 -filled glovebox, where the halide elpasolite films were deposited following the procedure detailed earlier.

The hole transport layer (HTL) used was poly[bis(4-phenyl)(2,4,6-trimethylphenyl)amine], or PTAA (EM Index). The additives used were a solution of 51.7 mg mL⁻¹ bis(trifluoromethane)sulfonimide lithium salt (Li-TFSI, 99% from Sigma Aldrich) in acetonitrile, and a solution of 100 μL mL⁻¹ 4-tert-butylpyridine (tBP, 96%, Sigma Aldrich) in toluene. The HTL solution was prepared in an N₂-filled glovebox by mixing together 10 mg PTAA, 16 μL Li-TFSI solution, and 20 μL tBP solution with 964 μL toluene. This solution was shaken until fully dissolved. The HTL was deposited by dropping 40 μL PTAA solution onto the halide elpasolite film and spun at 1500 rpm for 20 s. To complete the devices, 100 nm of gold was thermally evaporated on top of the devices.

The device area was defined by the 4.1 mm² apertured area in which the metal top electrode and bottom FTO electrode overlapped. Solar simulations were performed using a calibrated ABET Technologies Sun 2000 solar simulator, with *I*-*V* sweeps made using a Keithley 2623 A source-measure unit. EQE measurements were made using a 300 W Xenon lamp (ILC Technology) for the light source, which was focused through a Gemini-180 double monochromator (Jobin Yvon Ltd.), and the same Keithley source-measure unit was used to measure the photocurrent produced in the device.

Characterization of Cs₂AgSb_xBi_{1-x}Br₆ Thin Films: XRD measurements were performed using a PANalytical X'Pert Pro diffractometer using Ni-filtered Cu K_α X-rays ($\lambda = 1.5406 \text{ \AA}$). Diffractograms were obtained from 5°–70° 2 θ with a step size of 0.016°. SEM measurements were made using an LEO 1530 VP instrument. The acceleration voltage was 3 kV, with 10⁻⁵ Pa as the chamber vacuum. All samples had Au/Pd deposited on top to prevent charge accumulation, and this was deposited using an Emitech sputter coater (65 mA current for 7 s). PDS measurements were made according to previous reports, and these are detailed in ref. [39]. Samples were prepared on quartz substrates, and these immersed in a FC-72 Fluorinert (3M Company) medium. The sample was pumped with chopped monochromated light of different wavelengths, and a fixed wavelength continuous wave (cw) laser probe was passed through the refractive index gradient in the liquid medium, with a deflection proportional to the absorbance of the pump light at a particular wavelength by the sample. PL measurements were performed using an intensified charge-coupled device camera (iCCD) using an Andor iStar DH740 CCI-010 system connected to a grating spectrometer (Andor SR303i). The films, deposited on glass, were excited with a 400 nm wavelength pump laser, produced using a frequency-doubled Ti:sapphire laser (Spectra-Physics Solstice). The repetition rate was 1 kHz and the pulse length was ≈100 fs. The slit width in the spectrometer was 400 μm, exposure time 0.3 s, and the number of accumulations 15. TA spectroscopy measurements were performed using 355 nm wavelength pump pulses with a pulse width of ≈800 ps. These were provided by an electronically controlled, Q-switched Nd:YVO₄ laser (Innolas Picolo 25). Broadband probe pulses (380–620 nm wavelength) were generated by focusing an 800 nm wavelength fundamental laser onto a CaF₂ crystal (Eksma Optics, 5 mm) controlled by a digital motion controller (Mercury C-863 DC Motor Controller). The repetition rate of the pump pulses was 1 kHz, but the transmittance with and without pump excitation ($T_{\text{pump on}}$ and $T_{\text{pump off}}$) through the samples was collected at a rate of 500 Hz, which was controlled by a chopper wheel rotating. The transmitted pulses were collected by a monochrome line scan camera (JAI SW-4000M-PMCL; spectrograph, Andor Shamrock SR-163). These transmittances were used to calculate the TA signal intensity,
$$\frac{\Delta T}{T} = \frac{T_{\text{pump on}} - T_{\text{pump off}}}{T_{\text{pump off}}}$$

Aerosol-Assisted Post-Annealing: The films were post-treated in a custom-made stainless steel reactor at temperatures ranging from 100–150 °C in a well-ventilated fume hood. A 50:50 volume ratio of DMF and DMSO solvent was used for the process. After the films were placed in the preheated reactor, N₂ gas at a flow rate of 0.5 dm³ min⁻¹ was used to carry aerosols of the DMF:DMSO solvent into the reactor. The aerosol-assisted solvent treatment process was conducted for 5 min, after which the reactor was cooled down to room temperature. Post-treatment annealing was conducted in an N₂-filled glovebox and the films were annealed at 150 °C for 5 min.

Supporting Information

Supporting Information is available from the Wiley Online Library or from the author.

Acknowledgements

The authors would like to thank Dr. Sachin Dev Verma and Prof. Akshay Rao for useful discussions on charge-carrier kinetics in the elpasolite films. Z.L. would like to thank the Cambridge Trust. Y.-T.H. acknowledges funding from the Ministry of Education from the Taiwan Government. Z.L. and Y.-T.H. both thank Downing College Cambridge for support. L.M. and J.B. acknowledge funding from the QMUL EPSRC Impact Accelerator Account (no. EP/R511596/1) and Queen Mary Impact Fund. S.J.Z. acknowledges support from the Polish National Agency for Academic Exchange within the Bekker program (no. PPN/BEK/2020/1/00264/U/00001). R.L.Z.H. acknowledges funding from the Royal Academy of Engineering through the Research Fellowships scheme (no. RF\201718\1701), as well as the Kim and Juliana Silverman Research Fellowship at Downing College Cambridge.

Conflict of Interest

The authors declare no conflict of interest.

Data Availability Statement

The data that support the findings of this study are openly available in Imperial Research Data Repository at <http://dx.doi.org/10.14469/hpc/11108>, reference number 11108.

Keywords

double perovskites, elpasolite, photovoltaics, post-treatment annealing, thin films, trap states

Received: August 12, 2022

Revised: September 5, 2022

Published online: September 29, 2022

- [1] L. A. Muscarella, E. M. Hutter, *ACS Energy Lett.* **2022**, *7*, 2128.
- [2] F. Wei, Z. Deng, S. Sun, F. Zhang, D. M. Evans, G. Kieslich, S. Tominaka, M. A. Carpenter, J. Zhang, P. D. Bristowe, A. K. Cheetham, *Chem. Mater.* **2017**, *29*, 1089.
- [3] F. Wei, Z. Deng, S. Sun, F. Xie, G. Kieslich, D. M. Evans, M. A. Carpenter, P. D. Bristowe, A. K. Cheetham, *Mater. Horiz.* **2016**, *3*, 328.
- [4] N. Moody, S. Sesena, D. W. DeQuillettes, B. D. Dou, R. Swartwout, J. T. Buchman, A. Johnson, U. Eze, R. Brenes, M. Johnston, C. L. Haynes, V. Bulović, M. G. Bawendi, *Joule* **2020**, *4*, 970.
- [5] N. R. Wolf, B. A. Connor, A. H. Slavney, H. I. Karunadasa, *Angew. Chem. Int. Ed.* **2021**, *60*, 16264.
- [6] A. H. Slavney, T. Hu, A. M. Lindenberg, H. I. Karunadasa, *J. Am. Chem. Soc.* **2016**, *138*, 2138.
- [7] R. L. Z. Hoye, L. Eyre, F. Wei, F. Brivio, A. Sadhanala, S. Sun, W. Li, K. H. L. Zhang, J. L. MacManus-Driscoll, P. D. Bristowe, R. H. Friend, A. K. Cheetham, F. Deschler, *Adv. Mater. Interfaces* **2018**, *5*, 1800464.
- [8] D. Bartesaghi, A. H. Slavney, M. C. Gélvez-Rueda, B. A. Connor, F. C. Grozema, H. I. Karunadasa, T. J. Savenije, *J. Phys. Chem. C* **2018**, *122*, 4809.

- [9] Z. Jin, Z. Zhang, J. Xiu, H. Song, T. Gatti, Z. He, *J. Mater. Chem. A* **2020**, *8*, 16166.
- [10] S. R. Rondiya, R. A. Jagt, J. L. MacManus-Driscoll, A. Walsh, R. L. Z. Hoye, *Appl. Phys. Lett.* **2021**, *119*, 220501.
- [11] L. R. V. Buizza, L. M. Herz, *Adv. Mater.* **2021**, *33*, 2007057.
- [12] B. Wu, W. Ning, Q. Xu, M. Manjappa, M. Feng, S. Ye, J. Fu, S. Lie, T. Yin, F. Wang, T. W. Goh, P. C. Harikesh, Y. K. E. Tay, Z. X. Shen, F. Huang, R. Singh, G. Zhou, F. Gao, T. C. Sum, *Sci. Adv.* **2021**, *7*, eabd3160.
- [13] S. J. Zelewski, J. M. Urban, A. Surrente, D. K. Maude, A. Kuc, L. Schade, R. D. Johnson, M. Dollmann, P. K. Nayak, H. J. Snaith, P. Radaelli, R. Kudrawiec, R. Nicholas, P. Plochocka, M. Baranowski, *J. Mater. Chem. C* **2019**, *7*, 8350.
- [14] Z. Li, S. Kavanagh, M. Napari, R. G. Palgrave, M. Abdi-Jalebi, Z. Andaji-Garmaroudi, D. W. Davies, M. Laitinen, J. Julin, M. A. Isaacs, R. H. Friend, D. O. Scanlon, A. Walsh, R. L. Z. Hoye, *J. Mater. Chem. A* **2020**, *8*, 21780.
- [15] Y.-T. Huang, S. R. Kavanagh, D. O. Scanlon, A. Walsh, R. L. Z. Hoye, *Nanotechnology* **2021**, *32*, 132004.
- [16] M. T. Hörantner, H. J. Snaith, *Energy Environ. Sci.* **2017**, *10*, 1983.
- [17] V. Pecunia, L. G. Occhipinti, R. L. Z. Hoye, *Adv. Energy Mater.* **2021**, *11*, 2100698.
- [18] Y. Peng, T. N. Huq, J. Mei, L. Portilla, R. A. Jagt, L. G. Occhipinti, J. L. MacManus-Driscoll, R. L. Z. Hoye, V. Pecunia, *Adv. Energy Mater.* **2021**, *11*, 2002761.
- [19] A. M. Ganose, D. O. Scanlon, A. Walsh, R. L. Z. Hoye, *Nat. Commun.* **2022**, *13*, 4715.
- [20] B. Wang, N. Li, L. Yang, C. Dall'Agnese, A. K. Jena, T. Miyasaka, X. F. Wang, *J. Am. Chem. Soc.* **2021**, *143*, 14877.
- [21] J. Simfukwe, R. E. Mapasha, A. Braun, M. Diale, *MRS Adv.* **2017**, *357*, 3545.
- [22] Y. Liu, L. Zhang, M. Wang, Y. Zhong, M. Huang, Y. Long, H. Zhu, *Mater. Today* **2019**, *28*, 25.
- [23] A. Kumar, S. K. Swami, S. S. Rawat, V. N. Singh, O. P. Sinha, R. Srivastava, *Int. J. Energy Res.* **2021**, *45*, 16769.
- [24] X. Yang, Y. Chen, P. Liu, H. Xiang, W. Wang, R. Ran, W. Zhou, Z. Shao, *Adv. Funct. Mater.* **2020**, *30*, 2001557.
- [25] M. R. Filip, X. Liu, A. Miglio, G. Hautier, F. Giustino, *J. Phys. Chem. C* **2018**, *122*, 158.
- [26] Z. Zhang, Q. Sun, Y. Lu, F. Lu, X. Mu, S.-H. Wei, M. Sui, *Nat. Commun.* **2022**, *13*, 1.
- [27] S. Yoon, B. Fett, A. Frebel, S. Kroisl, B. Herbig, M. Widenmeyer, B. Balke, G. Sextl, K. Mandel, A. Weidenkaff, *Energy Technol.* **2022**, *10*, 2200197.
- [28] F. Wei, Z. Deng, S. Sun, N. T. P. Hartono, H. L. Seng, T. Buonassisi, P. D. Bristowe, A. K. Cheetham, *Chem. Commun.* **2019**, *55*, 3721.
- [29] N. J. Jeon, J. H. Noh, Y. C. Kim, W. S. Yang, S. Ryu, S. Il Seok, *Nat. Mater.* **2014**, *13*, 897.
- [30] M. Yang, Z. Li, M. O. Reese, O. G. Reid, D. H. Kim, S. Siol, T. R. Klein, Y. Yan, J. J. Berry, M. F. A. M. van Hest, K. Zhu, *Nat. Energy* **2017**, *2*, 17038.
- [31] W. A. Dunlap-Shohl, Y. Zhou, N. P. Padture, D. B. Mitzi, *Chem. Rev.* **2019**, *119*, 3193.
- [32] G. Longo, S. Mahesh, L. R. V. Buizza, A. D. Wright, A. J. Ramadan, M. Abdi-Jalebi, P. K. Nayak, L. M. Herz, H. J. Snaith, *ACS Energy Lett.* **2020**, *5*, 2200.
- [33] T. Du, S. R. Ratnasingham, F. U. Kosasih, T. J. Macdonald, L. Mohan, A. Augurio, H. Ahli, C. T. Lin, S. Xu, W. Xu, R. Binions, C. Ducati, J. R. Durrant, J. Briscoe, M. A. McLachlan, *Adv. Energy Mater.* **2021**, *11*, 2101420.
- [34] T. Du, T. J. Macdonald, R. X. Yang, M. Li, Z. Jiang, L. Mohan, W. Xu, Z. Su, X. Gao, R. Whiteley, C. T. Lin, G. Min, S. A. Haque, J. R. Durrant, K. A. Persson, M. A. McLachlan, J. Briscoe, *Adv. Mater.* **2022**, *34*, 2107850.
- [35] T. Du, F. Richeimer, K. Frohna, N. Gasparini, L. Mohan, G. Min, W. Xu, T. J. MacDonald, H. Yuan, S. R. Ratnasingham, S. Haque, F. A. Castro, J. R. Durrant, S. D. Stranks, S. Wood, M. A. McLachlan, J. Briscoe, *Nano Lett.* **2022**, *22*, 979.
- [36] H. Sun, G. W. P. Adhyaksa, E. C. Garnett, *Adv. Energy Mater.* **2020**, *10*, 2000364.
- [37] M. Winter, The Periodic Table of Elements, <https://www.webelements.com>, **1993**. (accessed: August 2022).
- [38] Z. Li, S. P. Senanayak, L. Dai, G. Kusch, R. Shiv, anna, Y. Zhang, D. Pradhan, J. Ye, Y. Huang, H. Siringhaus, R. A. Oliver, N. C. Greenham, R. H. Friend, R. L. Z. Hoye, *Adv. Funct. Mater.* **2021**, *31*, 2104981.
- [39] A. Sadhanala, F. Deschler, T. H. Thomas, E. Dutton, K. C. Goedel, F. C. Hanusch, M. L. Lai, U. Steiner, T. Bein, P. Docampo, D. Cahen, R. H. Friend, *J. Phys. Chem. Lett.* **2014**, *5*, 2501.